Study of three-body charged decays of K_L^0 †

C. D. Buchanan, D. J. Drickey, D. M. Pepper,* F. D. Rudnick, and P. F. Shepard‡
University of California at Los Angeles, Los Angeles, California 90024

E. Dally,§ P. Innocenti,|| E. Seppi¶
Stanford Linear Accelerator Center, Stanford, California 94305

C.-Y. Chien, B. Cox,** L. Ettlinger, L. Resvanis,†† and R. Zdanis
The Johns Hopkins University, Baltimore, Maryland 21218

(Received 14 August 1974)

An experiment using a wire-chamber magnetic spectrometer was performed at SLAC to obtain the form factors for K_L^0 decays. This experiment was designed to measure efficiently all three major decay modes $K_{3\pi}$, K_{e3}, and $K_{\mu 3}$ simultaneously. For the $K_{3\pi}$ decay, we measured the slope parameter $a = -4.69 \pm 0.17$. We find for the semileptonic modes K_{e3} and $K_{\mu 3}$ that $\lambda_+ = +0.044 \pm 0.006$, $\lambda_0 = +0.024 \pm 0.013$, and $\xi(t) = -0.20 \pm 0.15$. All the uncertainties quoted above include systematic effects.

I. INTRODUCTION

We report here a high-statistics measurement of the decay form factors of K_L^0 using a wire-chamber magnetic spectrometer. This particular experiment distinguishes itself from most others in that the same apparatus was used to accumulate data on all three major decay modes,

$$K_L^0 \to \pi^+\pi^-\pi^0 , \tag{1}$$

$$K_L^0 \to \pi^\pm e^\mp \nu , \tag{2}$$

$$K_L^0 \to \pi^\pm \mu^\mp \nu , \tag{3}$$

which will be referred to as $K_{3\pi}$, K_{e3}, and $K_{\mu 3}$ decays.

After all appropriate cuts, a sample of 56 000, 24 000, and 32 000 events were selected for the $K_{3\pi}$, K_{e3}, and $K_{\mu 3}$ decay modes, respectively. Experiments of this size are usually limited by systematic effects often due to unmeasured decay modes. Thus by measuring all three major modes simultaneously, there is an obvious advantage of being able to accumulate a large sample of data with which to study and eliminate systematic effects. We find good internal consistency in our experiment from cross checks of analyses of different decay modes.

We discuss the apparatus and trigger, Monte Carlo simulation, K_L^0 momentum spectrum, decay-mode separation, detection efficiency, and background in each mode in Secs. II through VII. The study of systematic effects is discussed in Sec. VIII.

We parametrized the Dalitz-plot density of $K_{3\pi}$ decay in the form[1]

$$\frac{dN}{dT_0} \propto |M|^2 \propto 1 + a\frac{Q}{M_K}\,Y + b\left(\frac{Q}{M_K}\right)^2 Y^2 , \tag{4}$$

where

M_K = K_L^0 rest mass,

T_0 = the kinetic energy of the π^0 in the K_L^0 rest frame,

$Q = \frac{3}{2} T_0^{\max}$,

$Y = (3T_0 - Q)/Q$.

Results of $K_{3\pi}$ decays are presented in Sec. IX.

We have analyzed the semileptonic K_L^0 decays [K_{l3}, Eqs. (2) and (3)] with Dalitz-plot density using the $V-A$ matrix elements which have been thoroughly documented and reviewed in the literature[2]:

$$\frac{d^2N}{dT_\pi dT_l} \propto |M|^2 \propto A f_+^2(t) + B f_+(t) f_-(t) + C f_-^2(t) , \tag{5}$$

where A, B, and C are known kinematic factors

$$A = M_K(2T_l T_\nu - M_K T'_\pi) + M_l^2(\tfrac{1}{4} T'_\pi - T_\nu) ,$$

$$B = M_l^2(T_\nu - \tfrac{1}{2} T'_\pi) ,$$

$$C = \tfrac{1}{4} M_l^2 T'_\pi .$$

Here M_K and M_π are the rest masses of K_L^0 and $\pi^\pm$; T_π, T_l, T_ν are the kinetic energy of the pion, charged lepton ($e^\pm$ or $\mu^\pm$) and neutrino in the K_L^0 rest frame; $T'_\pi = T_\pi^{\max} - T_\pi$; and $t = -(P_K - P_\pi)^2/M_\pi^2 > 0$, the dimensionless four-momentum transfer squared from K to π in units of M_π^2.

The functions to be determined are $f_+(t)$ and $f_-(t)$, two independent form factors. Since both B and C in Eq. (5) contain M_l^2, we can neglect these terms for the K_{e3} decay mode [Eq. (2)] and simplify its Dalitz-plot density to the form

$$\frac{d^2N}{dT_\pi dT_e} \propto A f_+^2(t) \ . \tag{6}$$

Thus the analysis of K_{e3} decays provides $f_+(t)$ directly. Results are presented in Sec. X.

In $K_{\mu 3}$ decays, all three terms in Eq. (4) contribute appreciably; therefore, $f_+(t)$ and $f_-(t)$ are measured simultaneously. Historically, their ratio

$$\xi(t) = f_-(t)/f_+(t) \tag{7}$$

was used to rewrite Eq. (5) as

$$\frac{d^2N}{dT_\pi dT_l} \propto f_+^2(t)[A + B\,\xi(t) + C\,\xi^2(t)] \ . \tag{8}$$

Again we are left with two independent functions to be determined.

A different form factor $f_0(t)$ has also been suggested,[2]

$$f_0(t) \equiv f_+(t) + \frac{t}{M_K^2/M_\pi^2 - 1} f_-(t) \ . \tag{9}$$

Then the Dalitz-plot density can be rewritten as

$$\frac{d^2N}{dT_\pi dT_l} \propto \alpha f_+^2(t) + \beta f_+(t) f_0(t) + \gamma f_0^2(t) \ , \tag{10}$$

where α, β, and γ are again known kinematic functions.

Here the independent form factors are $f_+(t)$ and $f_0(t)$. Theoretically, $f_+(t)$ and $f_0(t)$ are proportional to the transition amplitudes of the lepton lair $l\nu$ in definite spin-parity states: 1^- and 0^+, respectively.[2,3] Experimentally it is also advantageous to analyze in terms of $f_+(t)$ and $f_0(t)$ since they are less strongly correlated than $f(t)$ and $\xi(t)$.[3] Thus in this paper we emphasize the measurement of $f_+(t)$ and $f_0(t)$. Results are presented in Sec. XI, while the details of $K_{\mu 3}$ are presented in Appendix A. The conclusions of this experiment are presented in Sec. XII.

An experiment using the same spectrometer to measure K_L^0 form factors (referred to as experiment I) has been reported previously.[4] Results from these two experiments are compared in Appendix B.

Finally, results from the present experiment are compared with the world average in Appendix C.

II. BEAM APPARATUS AND THE TRIGGER

The K_L^0 beam was produced at the Stanford Linear Accelerater Center by a 16-GeV/c e^- beam impinging on a 21-in. long Be target. The neutral beam exiting at 3° with respect to incident electrons was collimated by a 12-ft concrete and steel shielding wall and subsequently passed through a 12-in. Pb filter to suppress photons. Two additional collimators and sweeping magnets were installed in the 152-ft space between the photon shield and the experimental apparatus.

The apparatus (Fig. 1) consisted of trigger counters, magnetic spectrometer, and electron and muon identifiers. Starting from the upstream end, they are the following:

(1) Two scintillation counts (A) and (T) defined the 2-m long decay volume.

(2) There were six wire spark chambers with magnetostrictive readout. Three of them were used for x-y coordinate readouts, and three were rotated by 45° to resolve ambiguities in track formation. These upstream chambers defined two charged tracks before they entered the analyzing magnet.

(3) A 72D36, 10.5-kG m analyzing magnet was used. The individual tracks determined in upstream chambers were tracked through this magnet and matched with corresponding tracks in the downstream chambers. The polarity of magnetic field was changed regularly to study possible systematic effects.

(4) Five more magnetostrictive readout wire spark chambers were used to determine x-y coordinates downstream of the magnet.

(5) There were two arrays of six trigger scintillation counters (called slats) with six horizontal ones immediately downstream of the six vertical ones. Since the analyzing magnet separated the two oppositely charged tracks in the horizontal plane, we triggered on the basis of a Left-Right coincidence. Three horizontal and three vertical slats on the left were fed to OR circuits separately and then formed a coincidence called (Left); the coincidence (Right) was similarly formed. The entire apparatus was then triggered by a coincidence

$$(\bar{A})\cdot(T)\cdot(\text{Left})\cdot(\text{Right}) \ ,$$

which defined a neutral particle decaying inside our decay volume with a charged decay product through each side of the spectrometer. This trigger, therefore, accepts all three decay modes:

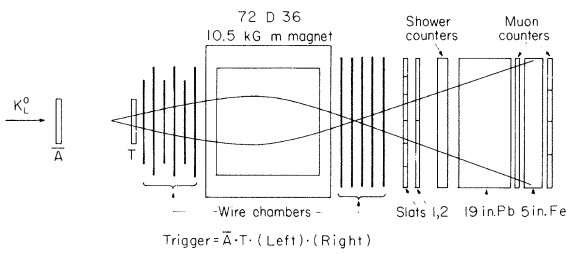

FIG. 1. Schematic diagram of the experimental apparatus.

$K_{3\pi}$, K_{e3}, and $K_{\mu 3}$.

(6) Four five-radiation length Pb-scintillation shower counters to identify electrons were used. The anode signal passed through a linear gate and stretcher, then to an ADC (analog-to-digital converter) which digitized the pulse heights on a scale of 0 to 256. A single muon had a pulse-height distribution which peaked at 40 and fell to zero by 60; pions peaked at 40 with ~20% of them above 80 due to hadronic interactions, while electrons peaked at 165 with ~10% of them below 128. These counters were not in the trigger, but their pulse heights are crucial to later data analysis for decay-mode separation. We required electrons to have pulse height ≥ 120 and muons and pions to have pulse height ≤ 80.

(7) Muon identification consisted of a block of 19-in. Pb and 5-in. steel with scintillation counters interspersed to register muons with momentum above 900 MeV/c. Pions and electrons were absorbed in the lead-steel shielding. Muon identification was not in the trigger but was latched and recorded on the data tape for later analysis.

(8) A Hewlett-Packard HP2116B computer was used to accumulate data on magnetic tape. The event data included spark-chamber coordinates, scintillation-counter latches, shower-counter pulse heights, and information for beam monitoring. The HP2116B was also used for on-line analysis, primarily to monitor efficiencies of counters and spark chambers. Approximately 420 000 K_L^0 decays were recorded with this system.

III. MONTE CARLO SIMULATION

A simulated data tape was generated with a Monte Carlo program which started with a K_L^0 source spread over the face of the photon filter. These kaons were then allowed to decay in the decay volume into one of three decay modes, $K_{3\pi}$, K_{e3}, and $K_{\mu 3}$, according to the appropriate K_L^0 lifetime, branching ratios, and matrix elements. The secondary tracks, including the photons from the π^0 in the $K_{3\pi}$ decays, were propagated through the entire system undergoing multiple scattering, electron bremsstrahlung, and pion decay. They were propagated through the magnetic field and induced appropriate pulse heights in the shower counters and latched the muon counters if they did not interact or range out in the muon wall. Suitable errors for wire spark-chamber position were also introduced on the charged tracks before the events were placed on tape. The identical format was used for both real and Monte Carlo data tapes so that they could be processed through the same analysis program. The distribution of the Monte Carlo data was compared with the real data in both geometric and kinematic variables to ensure that the Monte Carlo data properly represented the experimental data.

Two of the most sensitive tests for the Monte Carlo simulation were provided by the distribution in variables

$$P_0'^2 \equiv \frac{(M_K^2 - M_c^2 - M_0^2)^2 - 4(M_c^2 M_0^2 + M_K^2 P_T^2)}{4(P_T^2 + M_c^2)}, \tag{11}$$

$$\Delta P_T \equiv P_n - P_T \tag{12}$$

where M_K, M_0, and M_c are respectively the rest masses of K_L^0, π^0, and the charged pair interpreted as $\pi^\pm$; P_T is the transverse momentum of the charged pair; and P_n is the momentum of the neutral particle in the K_L^0 rest frame calculated according to a particular K_L^0 decay mode using the measured momentum vectors of the charged pair.

Note that characteristically $P_0'^2 > 0$ for $K_{3\pi}$ decays, $P_0'^2 \leq 0$ for K_{l3} decays, and that $\Delta P_T > 0$ if calculated for the correct decay mode without measuring error.

As an example of comparison, the $P_0'^2$ spectrum for all modes is shown in Fig. 2. Since the cal-

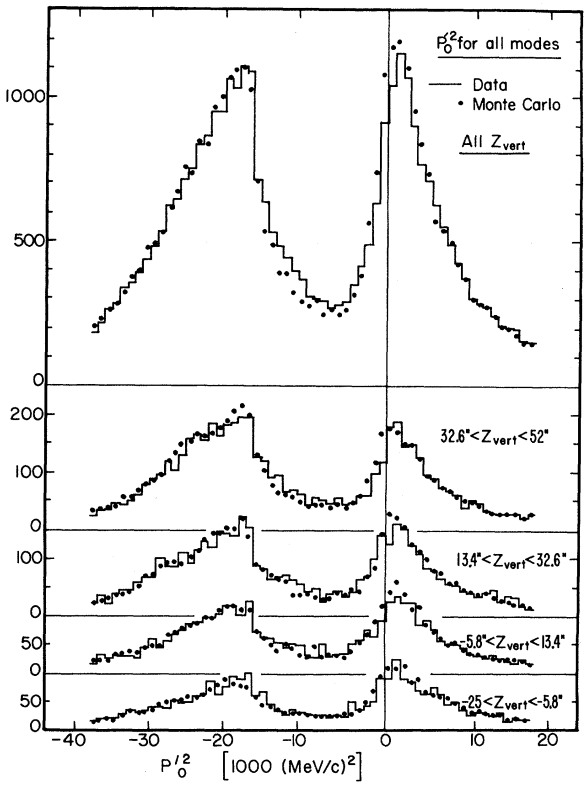

FIG. 2. $P_0'^2$ distribution for all decay modes. The solid lines are real data while the dots are Monte Carlo distributions. Also shown are distributions for different ranges of longitudinal positions of the K_L^0 decay vertex.

culation of $P_0'^2$ assumes the charged particles to be pions, mode separation is not involved in this comparison. Thus the agreement between all Monte Carlo data and all data simply confirms the knowledge of the geometry and the resolution of the apparatus. Since the efficiency of our system varies strongly with decay modes and decay position (see Sec. VI), we also show in Fig. 2 the $P_0'^2$ distributions for various vertex positions.

The variable ΔP_T depends on the correct identification of decay mode (see Sec. V) as well as proper reconstruction of kinematic variables. Figure 3 shows the ΔP_T distribution for the K_{e3} and $K_{\mu 3}$ modes. Also shown is the $P_0'^2$ distribution for the events identified as $K_{\mu 3}$ decays.

IV. K_L^0 BEAM MOMENTUM SPECTRUM

We used two methods to determine the spectrum of P_K, the laboratory momentum of K_L^0. The first was from a study of the $K_2^0 - K_1^0$ regeneration and subsequent $K_1^0 \to \pi^+\pi^-$ decays; the second was from a self-consistent treatment of 3π decays. At high values of P_K, both techniques agree. At low values of P_K, the $\pi^+\pi^-$ sample loses sensitivity because of the low acceptance due to its large Q value; thus only the spectrum from 3π decays was used (Fig. 4). Using this spectrum, it was found that the matrix element for each decay mode was independent of P_K.

V. SEPARATION OF DECAY MODES

The separation of decay modes was done on the basis of three kinds of criteria: geometric cuts, kinematic cuts, and particle identification. We first discuss the geometric cuts since they are shared by all decay modes, then discuss the other two cuts for each mode separation. All real and Monte Carlo events were processed by the same analysis programs. In the discussion below, the generic term data should be understood to mean both real and Monte Carlo events.

A. Geometric cuts for all decay modes

(1) A fiducial volume cut was imposed on the decay vertex to suppress interaction in the defining counters A and T.

(2) Tracks which came close to the magnet mirrors or yokes were rejected.

(3) The projected position of a charged track had to be more than 2 in. inside the physical boundary of the muon counters. Studies of multiple-scattering effects showed that this was necessary for low-momentum tracks.

(4) Slopes of the two charged tracks before the magnet had to be separated by more than 8 mrad to eliminate an observed bias due to spark coalescing of the magnetostrictive readout.

(5) All events were required to latch the aimed-at slat counters to ensure the electronic information being in time with the reconstructed tracks.

(6) All charged tracks had reconstructed mo-

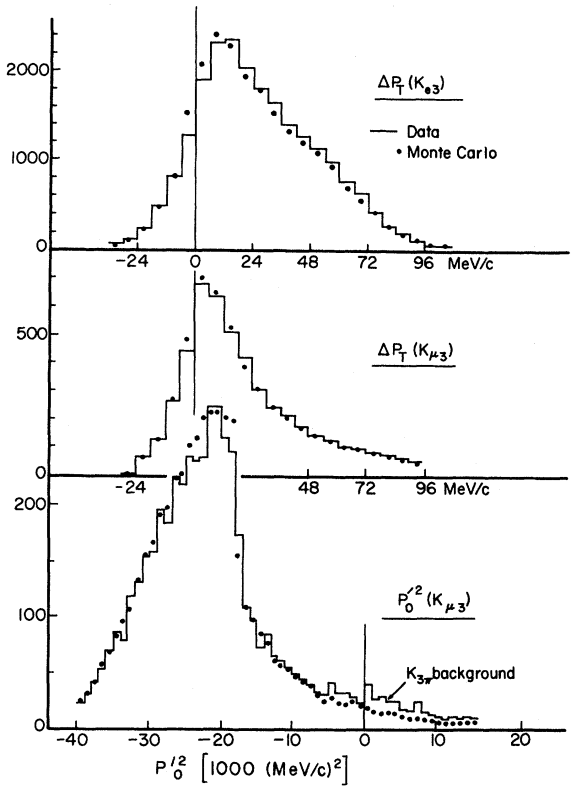

FIG. 3. Distribution of ΔP_T for K_{l3} decays and $P_0'^2$ distribution for $K_{\mu 3}$ decays. The dots are Monte Carlo distributions.

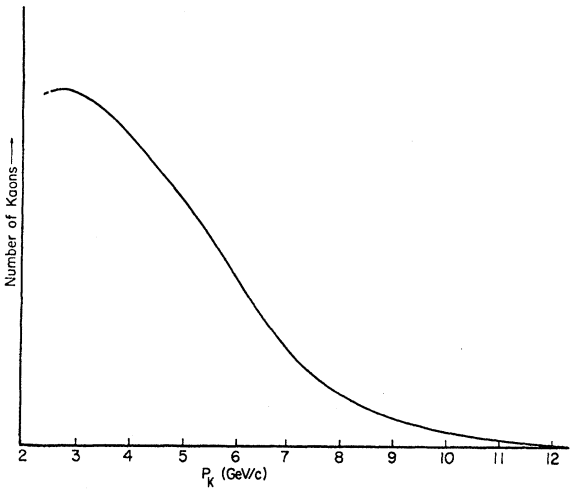

FIG. 4. Momentum spectrum of the K_L^0 incident on the detector at the decay volume.

menta greater than 900 MeV/c to ensure sufficient range for muon identification.

B. Selection of $K_{3\pi}$ mode

(1) Neither charged particle penetrated the lead-steel barrier.

(2) The transverse momentum of each charged track was less than 158 MeV/c.

(3) The transverse momentum P_T of the charged pair was consistent with 3π decay. A 25-MeV/c range in ΔP_T was allowed to account for experimental resolution, i.e., $\Delta P_T \geq -25$ MeV/c.

(4) $P_0'^2 > -5000$ (MeV/c)^2.

(5) No selection was made on shower-counter pulse heights because of the presence of photons from π^0 decays.

C. Selection of K_{e3} mode

(1) Neither charged track penetrated the lead-steel barrier.

(2) The transverse momentum of each charged track was less than 255 MeV/c.

(3) The transverse momentum P_T of the charged pair was consistent with K_{e3} decay within 25 MeV/c, i.e., $\Delta P_T \geq -25$ MeV/c.

(4) $P_0'^2 < -13\,000$ (MeV/c)^2.

(5) The pulse heights observed were consistent with a pion and an electron.

(6) Since the K_L^0 momentum for each decay was unknown, there were two possible entries on the Dalitz plot due to the quadratic ambiguity. In order to limit systematic effects due to the wrong solutions on the Dalitz plot, only events with both solutions within 20 MeV in the Dalitz plot were retained. This sample will be referred to as the "unambiguous" sample.

D. Selection of $K_{\mu 3}$ mode

(1) One and only one charged track penetrated the lead-steel barrier.

(2) The transverse momentum of each track was less than 236 MeV/c.

(3) P_T was consistent with $K_{\mu 3}$ decay within 25 MeV/c.

(4) The observed pulse heights were consistent with a pion and a muon.

(5) Only events with "unambiguous" solutions were retained.

(6) No selection was made on the variable $P_0'^2$. We find that a cut on $P_0'^2$ for the $K_{\mu 3}$ mode depletes mostly the high-T_ν corner of the Dalitz plot which contributes most to the interference term of the two form factors in Eqs. (5), (8), and (10). Therefore, we chose not to cut on $P_0'^2$ in order not to greatly reduce the sensitivity of our experiment to form factors $f_0(t)$ and $f_-(t)$.

Application of these cuts to the 410 000 recorded K_L^0 decays yielded ~56 000 events fully identified as $K_{3\pi}$ decays, ~24 000 identified as K_{e3}, and ~32 000 identified as $K_{\mu 3}$. About $\frac{2}{3}$ of the K_{e3} and $K_{\mu 3}$ decays satisfied the unambiguous cut—i.e., the two solutions due to the kinematic ambiguity lay within 20 MeV of each other in the Dalitz plot. Table I shows the effects of each cut.

TABLE I. Cuts used in the separation of decay modes. Numbers shown are events surviving each cut. [P_T in MeV/c, $P_0'^2$ in (MeV/c)^2].

Common cuts		Number of surviving events	
Good data		413 214	
Slope difference >8 mrad		315 464	
Vertex and mirror cuts		257 028	
Projected tracks intercept μ counters		224 971	
$P_\pm > 900$ MeV/c		209 943	
$K_{3\pi}$		K_{e3}		$K_{\mu 3}$	
No μ latches	113 841	No μ latches	113 841	Tracks intercept shower counters	180 346
$P_T < 158$	78 310	Tracks intercept shower counters	100 478	Proper pulse heights	63 007
$\Delta P_T < -25$	55 908	Proper pulse heights and $P_T < 255$	46 183	Tracks intercept different shower counters	46 912
$P_0'^2 > -5000$	55 653	$P_0'^2 < -13\,000$	24 918	One μ latch and $P_T < 236$	32 510
		$\Delta P_T < -25$	24 491	$\Delta P_T < -25$	32 078
Total accepted sample	55 653	Total accepted sample	24 491	Total accepted sample	32 078
		Unambiguous sample	14 481	Unambiguous sample	21 143

VI. DETECTION AND IDENTIFICATION EFFICIENCY

A Monte Carlo sample of $K_{3\pi}$ decays was generated with P_K spectrum of Fig. 4 and a uniform vertex distribution in the decay volume. Of this sample, 44% provided a valid trigger for the system; 56% of the surviving events satisfied all $K_{3\pi}$ cuts, leading to an over-all average efficiency of 24%.

A similar procedure was used for K_{e3} decays which yielded an efficiency of 20–30% for $P_K > 5$ GeV/c but a low efficiency for $P_K < 4$ GeV/c due to its large Q value. Overall, 8.5% provided a trigger; 45% of these passed K_{e3} cuts, yielding an over-all average efficiency of 3.8%. The unambiguous cut further reduced the efficiency to 2.4%.

For $K_{\mu 3}$ decays, 15% provided a trigger; 45% of these passed all $K_{\mu 3}$ cuts, giving an over-all efficiency of 6.9%. The unambiguous cut reduced it to 4.8%.

Figure 5 shows the efficiencies for $K_{3\pi}$ and unambiguous K_{e3} and $K_{\mu 3}$ decays as a function of positions on the Dalitz plot for each of the three modes.

VII. BACKGROUNDS

The major source of background for this experiment is a misidentification of the decay mode or a misidentification of the particles within the correct decay mode. Such contaminations were estimated by several cross checks. The discrimination of kinematic cuts alone against incorrect decay modes was studied using the Monte Carlo samples. These probabilities were combined with the measured counter efficiencies to yield an over-all efficiency for particle identification. These estimates were checked with the number of events observed in the sample with electron-electron, muon-muon, and pion-pion signatures.

An internally consistent set of probabilities was then established, yielding the identification matrix shown in Table II. The off-diagonal elements indicate misidentifications; i.e., contaminations. Only two important contaminations are observed: $(3.7 \pm 1)\%$ of the final $K_{3\pi}$ actually came from K_{e3} decays; $(3.8 \pm 1)\%$ of the final $K_{\mu 3}$ actually came from $K_{3\pi}$ decays. These rates were confirmed by the deviations of the $P_0'^2$ distributions from those expected of a pure sample.

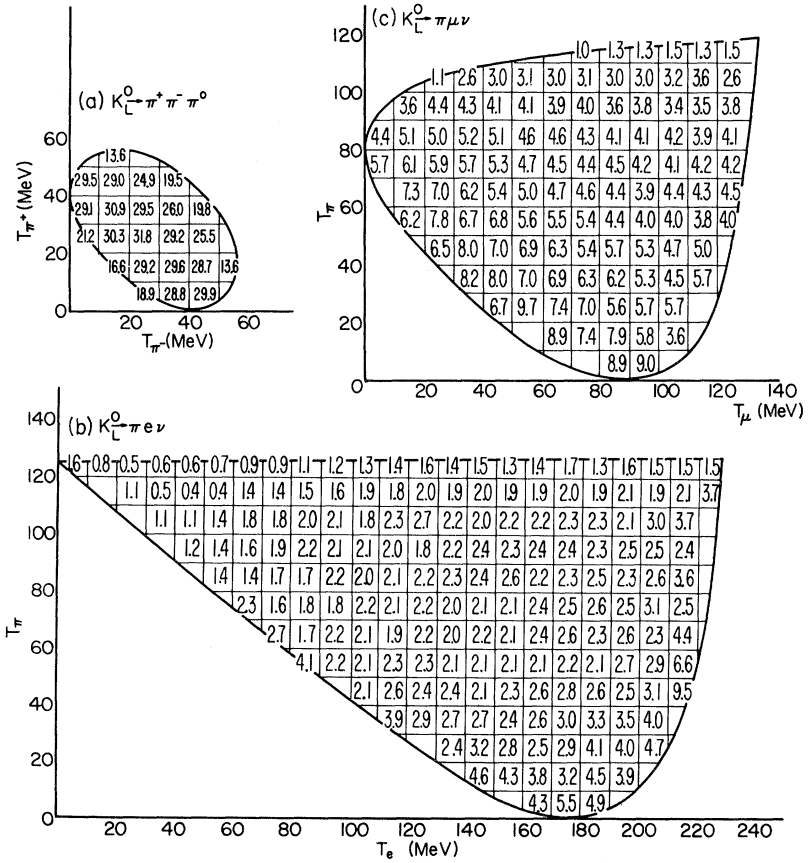

FIG. 5. Detection efficiencies in percentages over the Dalitz plots of the three decay modes.

All other background rates were small and were estimated to be known to ±50% of their values. The only other significant backgrounds were 0.8% $K_{\mu 3}$ and 0.5% $K_{e3}^{\rm rev}$ in the K_{e3} sample. (The latter is due to K_{e3} decays with pion and electron identification reversed.) These two contaminations have almost identical effects on the K_{e3} form factor: 1% of either background increases the slope λ_+^e of $f_+^e(t)$ by 0.0045.

VIII. THE STUDY OF THE SYSTEMATICS

Extensive effort was spent to understand the systematic effects and the self-consistency of our data. First the raw data tapes were divided evenly and processed independently at Johns Hopkins and UCLA. Analysis was done separately on these two samples and complete agreement was found for each decay mode. The total data was then divided into subsamples of different ranges of incident K_L^0 momentum and decay vertex position, different magnet polarities, and different lepton charges (for K_{e3} and $K_{\mu 3}$ decays). Analysis for each decay mode was performed on these subsamples to study the systematic effects. We also studied the effects due to the uncertainties in the P_K spectrum and the background subtraction, and variation of the $P_0'^2$ and ΔP_T cuts. Good consistency was found in all these studies.

Furthermore, we allowed events to extend beyond the exact kinematic limit in order to avoid bias at Dalitz-plot boundaries. Our experimental resolutions thus allowed a natural smearing across this boundary. We kept all events including the tail of the distribution and found that the Monte Carlo data had the same shape as the real data. The check on this procedure was to select only events at least 5 MeV inside the Dalitz-plot boundaries for both real data and Monte Carlo data and then to refit all the form factors. Results are consistent with those obtained from using the entire sample; therefore, we do not have problems at Dalitz-plot boundaries.

Uncertainties due to all these systematic effects are listed separately in Secs. IX to XI for each decay mode and they are included in the total uncertainties presented throughout this paper unless noted otherwise. We note that in each of the three modes the systematic uncertainty dominates the statistical uncertainty.

IX. ANALYSIS OF $K_{3\pi}$ DECAYS

After extracting the $K_{3\pi}$ sample from the data taken, as described above, a Dalitz plot, corrected for the K_{e3} background described in Sec. VII, was constructed. Monte Carlo events generated with the assumption of a constant matrix element were processed to produce a second Dalitz plot. The Monte Carlo events were corrected for the static Coulomb interaction between the π^+ and π^- (Ref. 5) by applying the multiplicative term $\eta/(e^\eta - 1)$, where $\eta = -2\pi\alpha/\beta$, α = fine structure constant, and $\beta = \vec{v}_+/c - \vec{v}_-/c$. The correction varied between 1.0 and 1.1 in our sample.

TABLE II. Identification matrix for different decay modes.

Actual source	Sample identified as K_{e3}	$K_{\mu 3}$	$K_{3\pi}$
K_{e3}	0.987	≤0.001	0.037
$K_{\mu 3}$	0.008	0.960	≪0.001
$K_{3\pi}$	≤0.001	0.038	0.963
$K_{l3}^{\rm rev}$	$K_{e3}^{\rm rev} = 0.005$	$K_{\mu 3}^{\rm rev} \leq 0.001$	···
Total	1.0	1.0	1.0

The square of the matrix element was measured by dividing the projection of the data Dalitz plot by the projection of the Monte Carlo distribution. The projections tested were T_0, T_+, X, and Y, where $X = (T_- - T_+)$ and $Y = (3T_0 - Q)/Q$. Figure 6 and Table III display the results as a function of T_0 quoting only statistical uncertainties.

As a check of the consistency of the data, they were divided into subsamples over limited decay volumes and also over limited ranges of kaon momentum P_K. These subsamples tested consistency because of the variations of the detection efficiency as a function of Dalitz-plot variables. Good consistency was obtained between the results extracted from the various subsamples. Table IV shows the results for the subsamples as a function of K_L^0 momentum.

For the full sample we observed no X dependence for the matrix element squared and chose to parametrize the results in the form of Eq. (4):

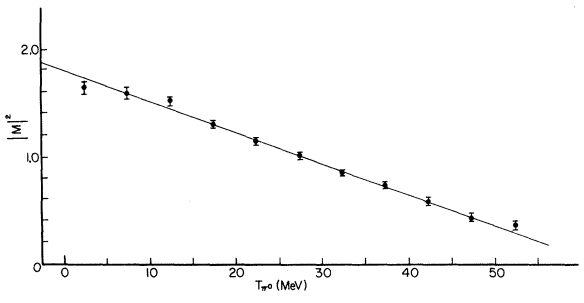

FIG. 6. Distribution of π^0 kinetic energy in K_L^0 rest frame. $|M|^2$ is the square of the matrix element. The straight line is the best linear fit with $a = -4.69$ (see text). Only statistical uncertainties are shown.

TABLE III. Matrix element $|M|^2$ as function of T_0 extracted from $K_{3\pi}$ decays and the results of linear and quadratic fits. (Uncertainties are statistical only.)

T_0 (MeV)	$\|M\|^2$
0–5	1.634 ± 0.046
5–10	1.595 ± 0.038
10–15	1.505 ± 0.032
15–20	1.298 ± 0.025
20–25	1.142 ± 0.021
25–30	1.012 ± 0.019
30–35	0.850 ± 0.016
35–40	0.732 ± 0.014
40–45	0.599 ± 0.013
45–50	0.445 ± 0.013
50–55	0.369 ± 0.024
Linear fit	
Slope $a = -4.69 \pm 0.08$	
χ^2/degrees of freedom = 13.7/9	
Quadratic fit	
Slope $a = -4.85 \pm 0.15$	
Slope $b = +2.9 \pm 1.7$	
χ^2/degrees of freedom = 7.6/8	

$$|M|^2 \propto 1 + a\frac{Q}{M_K}Y + b\left(\frac{Q}{M_K}\right)^2 Y^2 .$$

We find from a linear fit ($b \equiv 0$)

$$a = -4.69 \pm 0.17 ,$$

where the error includes systematic effects. A quadratic fit yields

$$a = -4.85 \pm 0.15 ,$$

$$b = +2.9 \pm 1.7$$

(statistical uncertainties only).

The systematic uncertainties include all the effects discussed in Sec. VIII. Their contributions to Δa are given in Table V. As is the usual case the systematic uncertainties dominate the statistical uncertainties.

TABLE IV. Values of slope parameter a as fitted from subsamples of different ranges of incident K_L^0 momentum P_K (statistical uncertainties only).

P_K (GeV/c)	Slope a	χ^2
<3	−4.47 ± 0.82	14.6
3–4	−4.50 ± 0.29	12.7
4–5	−4.50 ± 0.26	16.9
5–6	−4.76 ± 0.26	10.7
6–7	−5.32 ± 0.27	5.9
7–9	−4.82 ± 0.29	17.3
9–11	−6.69 ± 0.97	11.7
All	−4.69 ± 0.08	13.7

TABLE V. Contributions of systematic effects to the uncertainty in the slope parameter a in $K_{3\pi}$ decays.

Source of uncertainties	Δa
Background subtraction	±0.02
Position of $P_0'^2$ and ΔP_T cuts	±0.03
P_K spectrum variations	±0.07
Subsample variations	±0.13
Total systematics	±0.15
Statistics	±0.08
Total Δa	±0.17

Using the alternate parametrization

$$|M|^2 \propto 1 + 2a_0\frac{M_K}{M_0^2}(2T_0 - T_0^{\max}) + b_0\left[\frac{M_K}{M_0^2}(2T_0 - T_0^{\max})\right]^2 ,$$

the linear fit (including systematics) yields

$$a_0 = -0.277 \pm 0.010$$

and the quadratic fit (with statistical errors only) yields

$$a_0 = -0.286 \pm 0.009 ,$$

$$b_0 = +0.040 \pm 0.023 .$$

X. ANALYSIS OF K_{e3} DECAYS

Monte Carlo events were generated (see Sec. III) according to matrix element (6),

$$\frac{d^2N}{dT_\pi dT_e} \propto |M|^2 \propto A|f_+^e(t)|^2 , \qquad (6')$$

with $f_+^e(t) = 1$. The Monte Carlo data were then mixed with the background determined in Sec. VII (0.8% $K_{\mu 3}$ and 0.5% K_{e3}^{rev}). In addition, the radiative corrections of Ginsberg[6] and bremsstrahlung corrections to the measured electron momentum were applied.

Both the Monte Carlo and real data were then subjected to all K_{e3} cuts, including the unambiguous cut. Dalitz plots for unambiguous real and Monte Carlo data were thus obtained and compared with each other. Since the matrix element (6) used is proportional to $|f_+^e(t)|^2$, the agreement between Monte Carlo and real data for fixed-T_π (thus fixed-t) band is a measure of the validity of the $V-A$ theory, while the relative normalization of different T_π bands measures $f_+^e(t)$.

For each T_π band, the shape of the T_e spectrum

from the Monte Carlo calculation was compared with real data. Good agreement was obtained showing that the $V-A$ matrix element adequately describes the K_{e3} decay. From each band of fixed T_π (thus fixed t) the value of $|f_+^e(t)|^2$ was obtained by dividing the number of real events in each t band by the prediction from the Monte Carlo calculation in the same t band. This extraction has the important advantage that the only parametrization is that of the $V-A$ theory and can be fit to any t dependence later. Values of $f_+^e(t)$ are displayed in Fig. 7 and tabulated in Table VI.

This unparametrized form factor was then fit to the linear form

$$f_+(t) = f_+(0)(1+\lambda_+ t) \ . \qquad (13)$$

This fit yields

$$\lambda_+^e = +0.044 \pm 0.006 \ ,$$

which is indicated by the straight line in Fig. 7. This quoted uncertainty includes all the systematic effects discussed in Sec. VIII. Their individual contributions are listed in Table VII.

The agreement between the real data and the Monte Carlo distribution is shown in Fig. 8 by the T_e and T_π spectra. The K_{e3} detection efficiency as a function of t is also shown at the bottom of the figure. Results of quadratic fit and pole fit to the extracted $f_+^e(t)$ are shown in Table VI.

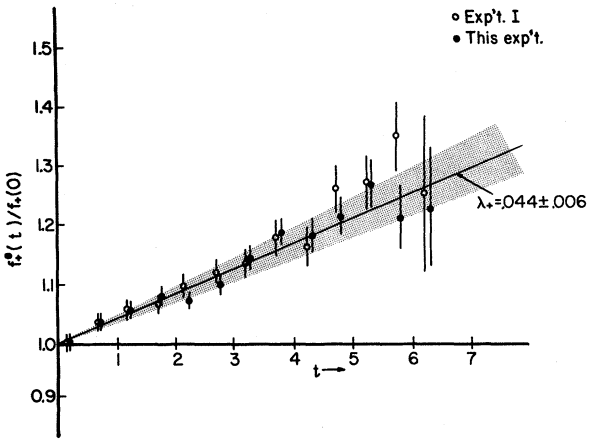

FIG. 7. The normalized form factor $f_+(t)/f_+(0)$ extracted from K_{e3} decays (solid circles). The straight line represents the best linear fit with the shaded band indicating the total uncertainty on λ_+. Only statistical uncertainties are shown on the data points. The results of experiment I are also shown (open circles).

As an internal check on the consistency of the data, the entire Dalitz plot was fitted without the requirement that both solutions be separated by less than 20 MeV. The results were consistent

TABLE VI. Values of the form factor $f_+^e(t)$ extracted from K_{e3} decays and the results of various fits to $f_+^e(t)$. (Only the uncertainty of the linear fit includes systematic effects. Values of χ^2 were based upon statistical uncertainties only. t is given in units of $M_\pi{}^2$.)

T_π (MeV)	t	$f_+^e(t)$
0–10	6.33	1.230 ± 0.098
10–20	5.82	1.213 ± 0.053
20–30	5.31	1.272 ± 0.040
30–40	4.80	1.217 ± 0.031
40–50	4.29	1.185 ± 0.027
50–60	3.78	1.190 ± 0.023
60–70	3.26	1.143 ± 0.020
70–80	2.75	1.098 ± 0.018
80–90	2.24	1.073 ± 0.016
90–100	1.73	1.084 ± 0.015
100–110	1.22	1.060 ± 0.013
110–120	0.71	1.038 ± 0.013
120–130	0.20	1.004 ± 0.015

Fit	$f_+(t)/f_+(0)$	Parameters	χ^2	Degrees of freedom
Linear	$1+\lambda_+ t$	$\lambda_+ = 0.044 \pm 0.006$	8.0	11
Quadratic	$1+\lambda_+ t+\lambda_+' t^2$	$\lambda_+ = 0.038 \pm 0.012$		
		$\lambda_+' = 0.001 \pm 0.002$	7.7	10
Pole	$\dfrac{1}{1-(M_\pi/M)^2 t}$	$M = 720 \pm 20$ MeV	8.7	11

with the unambiguous sample and yielded a value of $\lambda_+^e = 0.047$.

XI. ANALYSIS OF $K_{\mu 3}$ DECAYS

A Dalitz-plot distribution was constructed from the unambiguous $K_{\mu 3}$ sample as described in Sec. V. This Dalitz plot was corrected for the backgrounds [mainly $(3.8 \pm 1)\%$ $K_{3\pi}$ contamination; see Sec. VII], and by Ginsberg's radiative correction.[6] The Monte Carlo data were then fitted to the real data to extract the form factors. It is clear from Eq. (8) that for each fixed-T_π (thus fixed-t) band, the distribution depends at most on two real numbers, $f_+(t)$ and $\xi(t)$, which can be extracted directly from the T_μ spectrum of each T_π band. The extraction was performed with two different methods: a free fit and a band-coupled fit.

In the free fit, we determined $\xi(t)$ for each T_π band from the shape of its T_μ spectrum and determined $f_+(t)$ from the relative normalization of each T_π band. This free fit extracted both $f_+(t)$ and $\xi(t)$ without any *a priori* assumptions about the t dependence of these form factors. Details of this fit are presented in Appendix A. When this extracted f_+^μ was fitted to a linear t dependence [Eq. (13)], we obtained the slope

$$\lambda_+^\mu = +0.046 \pm 0.030$$

in agreement with λ_+^e.

In the band-coupled fit, we used $f_+^e(t)$ obtained from K_{e3} analysis (Sec. X) to demand smooth variation of $f_+^\mu(t)$, thus coupling different t bands. This procedure greatly restricts the fit and extracts $\xi(t)$ and $f_0(t)$ in unparametrized form while at the same time it does not depend on the exact form of $f_+(t)$ used within a reasonable range. The procedure and results are as follows.

We first chose a linear form of $f_+(t)$ from our K_{e3} analysis (i.e., $\lambda_+ = 0.044 \pm 0.012$) and an over-all normalization between the Monte Carlo data and the real data. Within each of the 12 bands of constant t, $\xi(t)$ was varied until a χ^2 was minimized for that t band. These 12 χ^2 were summed to give an over-all χ^2. The normalization was then varied and the process was repeated until a best over-all χ^2 was obtained. This yielded the best set of 12 values of $\xi(t)$ associated with the original input of $f_+(t)$. The central values of $f_0(t)$ were obtained from Eq. (9) using extracted values of $\xi(t)$ and input values of $f_+(t)$.

The input structure of $f_+(t)$ was then varied to study correlations between the input $f_+(t)$ and extracted $\xi(t)$ and $f_0(t)$. The detailed results are presented in Appendix A. We emphasize that it is a crucial aspect of this analysis that the varying assumptions for $f_+(t)$ change $\xi(t)$ and $f_0(t)$ by less than the statistical uncertainties.

TABLE VII. Contributions of systematic effects to the uncertainty in the linear slope parameter λ_+ of $f_+(t)$ in K_{e3} decays.

Source of uncertainties	$\Delta\lambda_+$
Effects of subsample variations	±0.002
P_K spectrum	±0.002
Background subtraction	±0.003
Position of $P_0'^2$ cut	±0.002
Position of ΔP_T cut	±0.002
Radiative corrections	±0.002
Total systematic	±0.005
Statistics	±0.003
Total $\Delta\lambda_+$	±0.006

Form factors $\xi(t)$ and $f_0(t)$ extracted from this band-coupled fit are displayed in Figs. 9 and 10. They are also tabulated in Table VIII. The correlations between changes in $f_+(t)$ and results have been propagated into the uncertainties shown for $\xi(t)$ and $f_0(t)$. Their contributions and those of the systematic effects (Sec. VIII) to $\Delta\xi(t)$ and

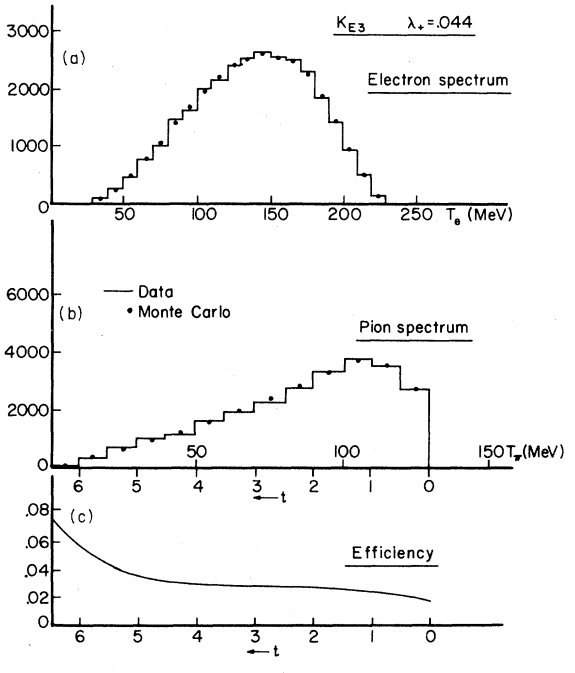

FIG. 8. Distributions of the kinetic energy of (a) the electron and (b) the pions in the K_L^0 rest frame for K_{e3} decays. (c) The detection efficiency for K_{e3} decays as a function of t.

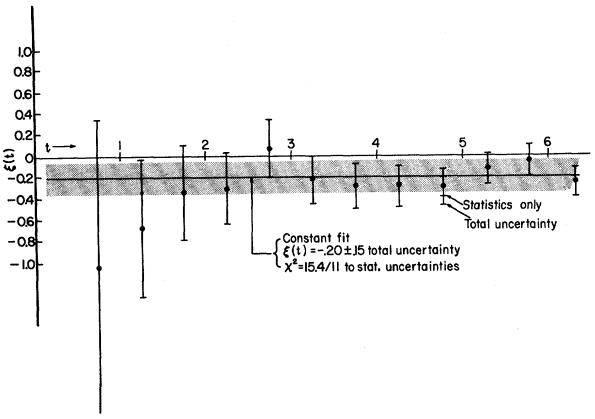

FIG. 9. The form factor $\xi(t)$ extracted from the band-coupled fit of $K_{\mu 3}$ decays using $f_+^e(t)$ as input. The error bar on each data point indicates the total uncertainty. The statistical error is shown in one of the high-t bins, and it increasingly dominates the errors of low-t bins. The straight line indicates the best fit to a constant, with the shaded band representing its total uncertainty.

$\Delta f_0(t)$ at a typical value of $t-4$ are listed in Table IX.

Table X summarizes the results of various fits to the extracted values of $\xi(t)$ and $f_0(t)$. The uncertainties quoted include all systematic contributions mentioned above, while the χ^2 quoted is based on statistical error only.

A constant fit to $\xi(t)$ yielded

$$\xi(t) = -0.20 \pm 0.15 ,$$

while a linear fit did not materially improve the fit.

A linear fit can be made of $f_0(t)$ with or without

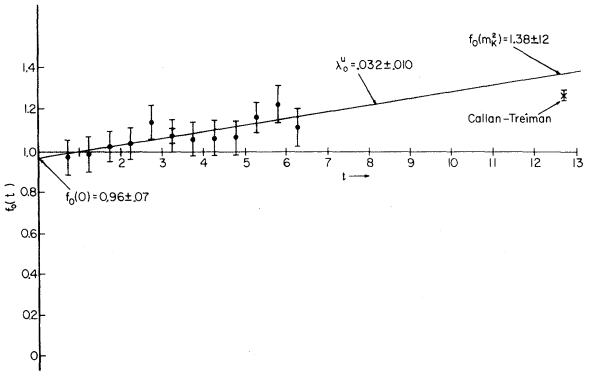

FIG. 10. The form factor $f_0(t)$ extracted from the band-coupled fit of $K_{\mu 3}$ decays using $f_+^e(t)$ as input. The error bar on each data point indicates its total uncertainty. The straight line represents the best unconstrained fit to $f_0(t)$ with the shaded band indicating its total uncertainty. The best constrained fit yields $\lambda_0 = 0.024 \pm 0.013$ (see text).

TABLE VIII. Values of form factors $\xi(t)$ and $f_0(t)$ extracted from the band-coupled fit of $K_{\mu 3}$ decays with $f_+(t)$ as input. [The uncertainties shown include systematic errors. χ^2/degrees of freedom shown are for the fit of $\xi(t)$ for each t bin; $f_0(t)$ is calculated from the fitted $\xi(t)$ and input $f_+^e(t) = 1 + 0.044t$.]

t	$\xi(t)$	$f_0(t)$	χ^2/d.f.
0.71	-1.05 ± 1.40	0.966 ± 0.084	0.5/2
1.22	-0.68 ± 0.77	0.980 ± 0.085	3.1/4
1.73	-0.35 ± 0.47	1.019 ± 0.073	5.8/6
2.24	-0.31 ± 0.36	1.032 ± 0.074	1.7/9
2.75	$+0.06 \pm 0.30$	1.136 ± 0.078	13.2/10
3.26	-0.23 ± 0.24	1.071 ± 0.076	8.1/11
3.78	-0.29 ± 0.23	1.056 ± 0.032	17.8/11
4.29	-0.29 ± 0.21	1.060 ± 0.085	6.4/11
4.80	-0.30 ± 0.19	1.061 ± 0.081	7.4/11
5.31	-0.13 ± 0.16	1.161 ± 0.075	15.1/11
5.82	-0.05 ± 0.16	1.224 ± 0.087	4.2/9
6.33	-0.24 ± 0.15	1.111 ± 0.090	4.8/6

the constraint that $f_0(0) = 1.0$. An unconstrained fit yielded

$$f_0(0) = 0.96 \pm 0.07 ,$$
$$\lambda_0 = 0.032 \pm 0.010 ,$$

which gave $f_0(M_K^2/M_\pi^2) = 1.38 \pm 0.12$ in good agreement with the Callan-Treiman prediction that $f_0(M_K^2/M_\pi^2) = 1.27 \pm 0.03$ and $\lambda_0 = +0.021 \pm 0.003$.[7] The agreement of $f_0(0)$ with 1.0 is a check on the self-consistency of the experiment and analysis. Therefore it is justified to constrain $f_0(0) = 1.0$ and this constrained fit yielded

$$\lambda_0^c = 0.024 \pm 0.013 ,$$

consistent with the unconstrained fit. This fit gave $f_0(M_K^2/M_\pi^2) = 1.30 \pm 0.16$ which is again consistent with the Callan-Treiman prediction.

TABLE IX. Contributions of systematic effects to the uncertainties in extracted form factors $\xi(t)$ and $f_0(t)$ at $t = 4$ in the band-coupled $K_{\mu 3}$ fit.

Source of uncertainties	$\Delta\xi(t)$	$\Delta f_0(t)$
Background subtraction	±0.05	±0.02
Position of ΔP_T cut	±0.05	±0.02
P_K spectrum variations	±0.06	±0.03
Subsample variations	±0.05	±0.02
$\Delta\lambda_+$ (f_+ shape)	±0.05	±0.02
f_+ normalization	±0.10	±0.04
Total systematics	±0.16	±0.06
Statistics	±0.10	±0.05
Total	±0.19	±0.08

Table X summarizes these results and Table XI lists contributions to $\Delta\lambda_0$.

XII. CONCLUSIONS

Our main results for each major decay mode (including systematic effects) are the following:

(1) The $K_{3\pi}$ analysis yields the results in Table III and Fig. 6 which are fitted to slope parameters

$$a = -4.69 \pm 0.17 \text{ or } a_0 = -0.277 \pm 0.010 .$$

(2) The K_{e3} analysis yields the unparametrized form factor $f_+(t)$ in Table VI and Fig. 7 which, when fitted to a linear t dependence, yields

$$\lambda_+^e = +0.044 \pm 0.006 .$$

(3) The band-coupled analysis of $K_{\mu 3}$ decays yields the extracted values of $\xi(t)$ and $f_0(t)$ in Table VIII and Figs. 9 and 10. $\xi(t)$ was fitted to a constant

$$\xi(t) = -0.20 \pm 0.15 .$$

A constrained fit to $f_0(t)$, with $f_0(0) = 1$, yields

$$\lambda_0 = +0.024 \pm 0.013$$

and results in $f_0(M_K^2/M_\pi^2) = 1.30 \pm 0.16$ in good agreement with Callan-Treiman predictions.

We note the following self-consistency in our analysis. Values of λ_+ obtained from K_{e3} and $K_{\mu 3}$ decays are consistent, $f_0(t)$ extrapolates to $f_0(0) = 1$, and the values of $\xi(t)$ and $f_0(t)$ obtained in the free fit are consistent with those from the band-coupled fit in $K_{\mu 3}$ decays.

XIII. ACKNOWLEDGMENT

The generous and willing cooperation of the staff at the Stanford Linear Accelerator Center is gratefully acknowledged.

Note added in proof. We are shocked and distressed by the death of our colleague, Darrell J. Drickey.

APPENDIX A: DETAILED RESULTS OF $K_{\mu 3}$ ANALYSIS

The band-coupled fit was done for $K_{\mu 3}$ data to extract $\xi(t)$ and $f_0(t)$ with different input forms of $f_+(t)$: the linear fit ($\lambda_+ = 0.044$) and quadratic fit from our K_{e3} analysis, and the world average[8] linear fit ($\lambda_+ = 0.032$). Figure 11 shows that the extracted form factors using these different input forms of $f_+(t)$ are consistently well within the uncertainty of each data point. We also varied the over-all normalization of the fit (estimated to be $\leq 3.5\%$) since it is coupled with the input $f_+(t)$. We found that the effect due to uncertainty in normalization was also small. The effects on fitted values from form factors $\xi(t) =$ constant, λ_0, and $f_0(0)$ are also very small, as is shown in Table XII.

TABLE X. Results of different fits to form factors $\xi(t)$ and $f_0(t)$ extracted from the band-coupled $K_{\mu 3}$ fit. (The quoted uncertainties include all systematic effects and correlations.)

$\xi(t)$	χ^2/degree of freedom
Constant fit: $\xi = -0.20 \pm 0.15$	15.4/11
Linear fit: $\xi(0) = -(0.34 \pm 0.31) + (0.03 \pm 0.07)t$	13.9/10

	$f_0(t)$	
	Unconstrained	Constrained
$f_0(0)$	0.96 ± 0.07	1.0 (input)
$f_0(M_K^2/M_\pi^2)$	1.38 ± 0.12	1.30 ± 0.16
λ_0	$+0.032 \pm 0.010$	$+0.024 \pm 0.013$
χ^2/degree of freedom	12.6/10	14.0/11

The results of $f_+(t)$, $\xi(t)$, and $f_0(t)$ of a free fit to our present data are shown in Fig. 12, and fits to these data are listed in Table XII. The free fit to our previous experiment I and band-coupled present results are also shown for comparision. A linear fit to the present $f_+^\mu(t)$ extracted from the free fit yields

$$\lambda_+^\mu = +0.046 \pm 0.030$$

(statistical uncertainty only) ,

TABLE XI. Contributions to $\Delta\lambda_0$.

Source of uncertainties	$\Delta\lambda_0$ Unconstrained	$\Delta\lambda_0$ Constrained
Statistics	±0.008	±0.004
$f_+(t)$ input structure	±0.005	±0.011
Other systematic effects (Sec. VIII)	±0.004	±0.005
Total	$\Delta\lambda_0^\mu = \pm 0.010$	$\Delta\lambda_0^e = \pm 0.013$

in good but weak agreement with λ_+^e. A constant fit to the free-fit results yields $\xi(t) = -0.29 \pm 0.16$ (statistical error only), with $\chi^2 = 13.4$ for 11 degrees of freedom, in good agreement with the band-coupled result of -0.20. A fit to the form factor $f_0(t)$ yields $\lambda_0^c = 0.026 \pm 0.012$ (statistical error only).

The band-coupled fit using the result of $\lambda_+^\mu = 0.046 \pm 0.030$ obtained from the $K_{\mu 3}$ free fit was also performed, and this yielded, including systematic uncertainties,

$$\lambda_0^c = +0.025 \pm 0.019$$

and

$$\xi(t) = -0.20 \pm 0.22$$

from a constant fit.

The values of $f_+(t)$ and $\xi(t)$ for a given band are highly coupled. Note the correlation [e.g., at $t = 2.25$ in Figs. 12(a) and 12(b)] for a high value of $\xi(t)$ to be coupled with a low value for $f_+(t)$. The introduction of band coupling cuts off these correlated excursions, as can be seen in Fig. 12. The band-coupled values tend to average the free-fit excursions.

APPENDIX B: COMPARISON OF THE PRESENT EXPERIMENT AND OUR PREVIOUS EXPERIMENT

The results of our previous experiment on K_L^0 form factors have been reported in the literature.[4] Here we compare those previous results with our present results. In the following, our earlier results from the Johns Hopkins–UCLA–SLAC Collaboration will be referred to as experiment I.

1. $K_{3\pi}$ decays

Experiment I yielded

$$a = -4.42 \pm 0.85 \quad \text{(statistical error only)}.$$

This value should be subjected to two modifications. The static Coulomb correction would lower it by 0.09; the correction due to K_L^0 momentum spectrum (see below) would also lower it.

We find for this experiment a P_K spectrum, in Sec. IV, which is somewhat more copious for $P_K < 3.5$ GeV/c than the spectrum for experiment I. The latter was obtained only from regenerated $\pi^+\pi^-$ decays which have low efficiency for low P_K (see Fig. 13). This difference has negligible effect on K_{e3} and $K_{\mu 3}$ results since the apparatus has

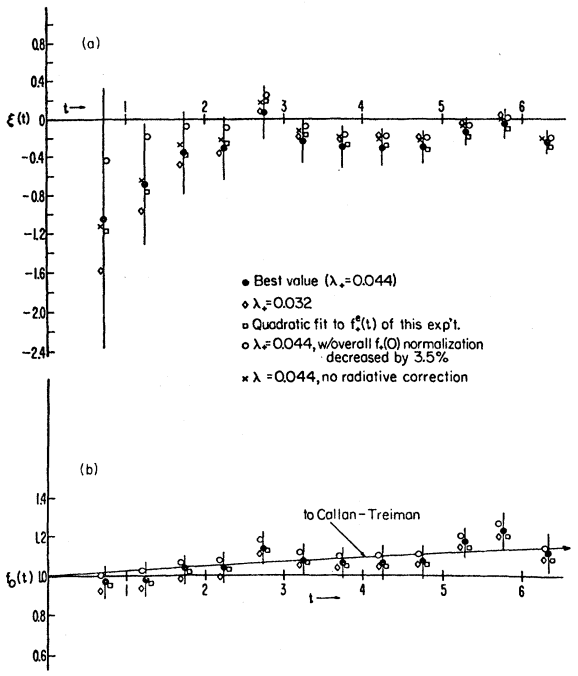

FIG. 11. Form factors (a) $\xi(t)$ and (b) $f_0(t)$ extracted from the band-coupled fit of $K_{\mu 3}$ decays using different forms of $f_+(t)$ as input: best value of $\lambda_+ = 0.044$ from our K_{e3} analysis (dots), world average of $\lambda_+ = 0.032$ (diamonds), quadratic fit to our $f_+^e(t)$ (squares), $\lambda_+ = 0.044$ with over-all $f_+(0)$ normalization decreased by 3.5% (circles), and $\lambda_+ = 0.044$ with no radiative correction (crosses).

TABLE XII. Effects on extracted $\xi(t)$ and $f_0(t)$ due to different forms of $f_+(t)$ input to the band-coupled $K_{\mu 3}$ fit. (The last entry lists results from a free fit of $K_{\mu 3}$ data; see text.)

Form of the input $f_+(t)$	$\xi(t)$ = constant	λ_0^μ	$f_0(0)$	λ_0^c
Linear with $\lambda_+ = 0.044$ (from K_{e3} fit)	−0.20	0.032	0.96	0.024
Linear with $\lambda_+ = 0.032$ (world average)	−0.19	0.037	0.92	0.017
Quadratic (from K_{e3} fit)	−0.20	0.029	0.95	0.020
$f_+(t)$ normalization reduced by 3.5%	−0.09	0.030	1.01	0.034
Linear with $\lambda_+ = 0.046$ (from $K_{\mu 3}$ free fit)	-0.20 ± 0.22	0.030 ± 0.023	0.97 ± 0.11	0.025 ± 0.019
Results of $K_{\mu 3}$ free fit	-0.29 ± 0.16	0.043 ± 0.036	0.95 ± 0.11	0.026 ± 0.012

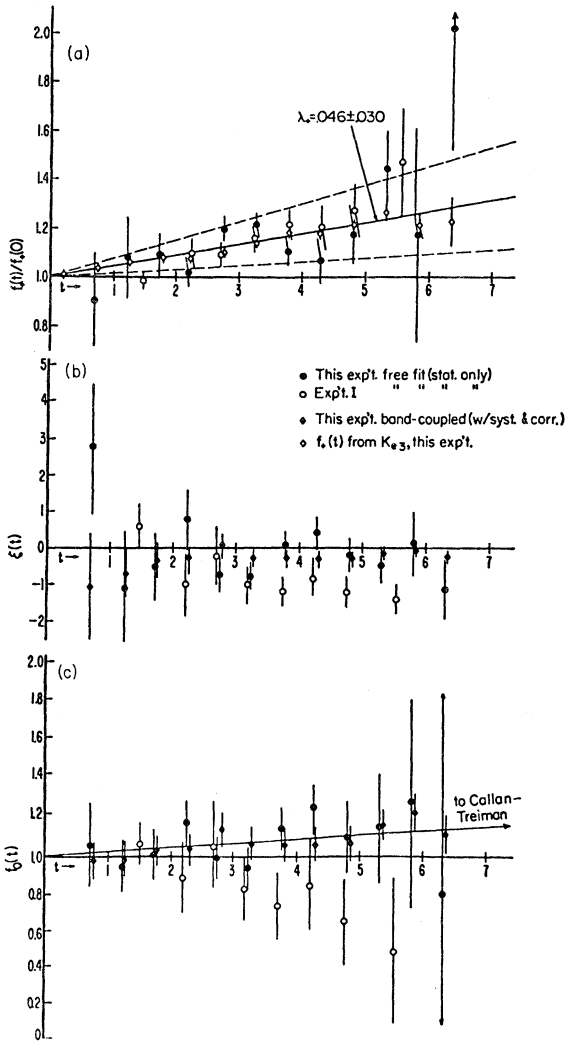

FIG. 12. Form factors (a) $f_+(t)$, (b) $\xi(t)$, and (c) $f_0(t)$ extracted from the free fit of $K_{\mu 3}$ decays (see text). Also shown are the results from a free fit of experiment I (circles), and from the band-coupled fit (solid diamonds) of this experiment. Figure 12(a) also shows $f_+(t)$ extracted from our K_{e3} analysis. Only the band-coupled results (solid diamonds) display total uncertainties.

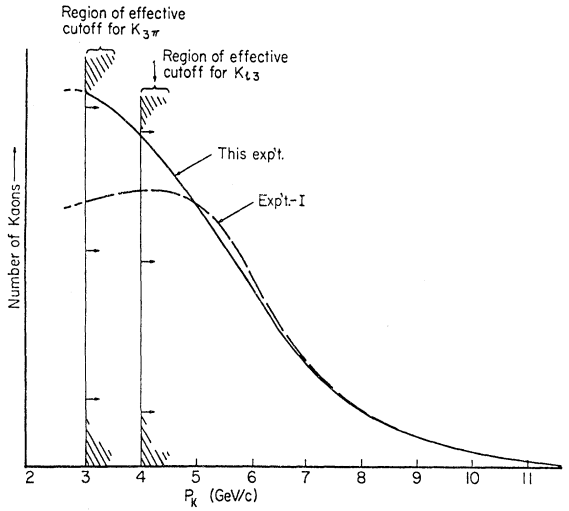

FIG. 13. Incident K_L^0 momentum spectrum used in this experiment (solid curve) and in experiment I (dashed curve).

decreasing efficiency for K_{e3} and $K_{\mu 3}$ with lower P_K due to their Q values; e.g., using the new spectrum for our old data would lower its λ_+^e by 0.002 and would lower $\xi(t)$ typically by ~0.1 for all t.

However, the effect of the P_K spectrum on $K_{3\pi}$ results is significant. The P_K spectrum obtained in this experiment should also be used in experiment I; this lowers our previously reported value of a by 0.20. Furthermore, the systematic uncertainties of our previous experiment should be at least comparable to those of this experiment as listed in Table V.

Combining all these effects, we find a corrected result for experiment I of

$$a = -4.71 \pm 0.17 ,$$

or

$$a_0 = -0.278 \pm 0.010 ,$$

which includes estimated systematic uncertainties. These are in excellent agreement with our new results

$$a = -4.69 \pm 0.17 ,$$

or

$$a_0 = -0.277 \pm 0.010 .$$

2. K_{e3} decays

Our previous experiment yielded $\lambda_+^e = +0.05 \pm 0.01$ in good agreement with the present result of $\lambda_+^e = 0.044 \pm 0.006$. [See Fig. 7 for detailed comparisons of the extracted form factor $f_+(t)$].

3. $K_{\mu 3}$ decays

Only a free fit was performed in experiment I extracting $f_+(t)$ and $\xi(t)$ for each t band. A detailed comparison with the present free-fit results (Fig. 12 in Appendix A) indicated that they are statistically compatible for $t \leq 3.5$. However, with $t > 3.5$, the values from experiment I of $\xi(t)$ are about two standard deviations below those of our new results.

Thus, these high-t points are responsible for both the lower average value of $\xi(t)$ and the higher value of λ_+^μ found in experiment I. The present

experiment is the better experiment; it benefits from higher precision, greater experience, and better internal consistency. However, the comparison and reexamination of our previous data have not found any specific corrections which should be made to experiment I. Thus, though the results differ somewhat from those of this experiment, the experiment I free-fit $K_{\mu 3}$ results for $f_+(t)$, $\xi(t)$, and $f_0(t)$ should continue to stand as an independent experiment.

APPENDIX C: COMPARISON WITH OTHER K_L^0 DALITZ-PLOT FORM FACTOR EXPERIMENTS

We compare here our present results with K_L^0 form factors obtained from other recent high-statistics experiments.

1. $K_{3\pi}$

The 1974 Particle Data Group compilation[9] summarized the world data on $K_L^0 \to 3\pi$ decays in the following parametrization:

$$|M|^2 = 1 + g(S_3 - S_0)/M_+^2 ,$$

where

$$S_3 = (M_K - M_0)^2 - 2M_K T_0 ,$$

$$S_0 = \tfrac{1}{3}(M_K^2 + 2M_+^2 + M_0^2) ,$$

with M_K, M_+, and M_0 denoting the rest mass of K_L^0, π^+, and π^0, respectively. The world average is

$$g = 0.610 \pm 0.021 ,$$

which gives

$$a_0 = -0.285 \pm 0.010$$

or

$$a = -4.83 \pm 0.17 .$$

The results from our experiment give

$$g = 0.590 \pm 0.022$$

or

$$a_0 = -0.277 \pm 0.010$$

or

$$a = -4.69 \pm 0.17 .$$

Figure 14 summarizes the results of $K_L^0 \to \pi^+\pi^-\pi^0$ form factors as compiled in Ref. 9 together with our present results and the revised results of experiment I.

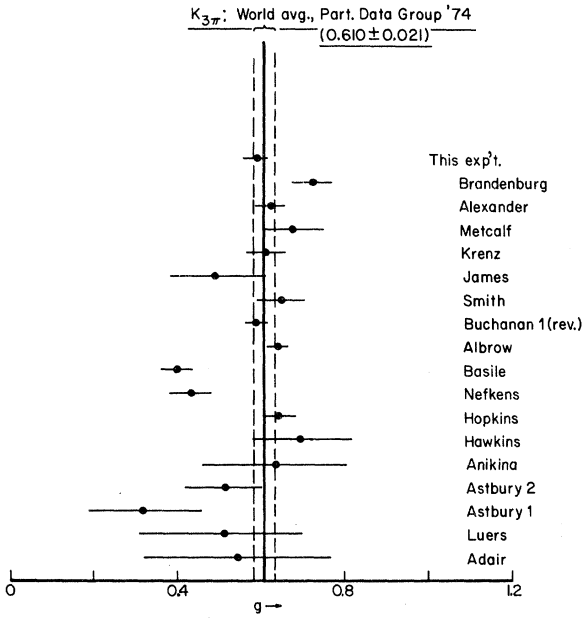

FIG. 14. World results of the slope parameter in $K_{3\pi}^0$ decays as compiled in Ref. 9 together with our present result and the revised result of experiment I.

2. $f_+(t)$

$f_+(t)$ is the only form factor in K_{e3} which can be studied without interference from a second form factor. Its structure has recently been reviewed by the SLAC–Santa Cruz Collaboration in terms of λ_+.[8] They find a world average value (including our present experiment) of

$$\lambda_+^e = 0.032 \pm 0.004 ,$$

but with a χ^2 of 28 for 13 degrees of freedom. Our present result of 0.044 ± 0.006 is ~ 2 standard deviations above this average value. We note also the preliminary result from the CERN-Heidelberg

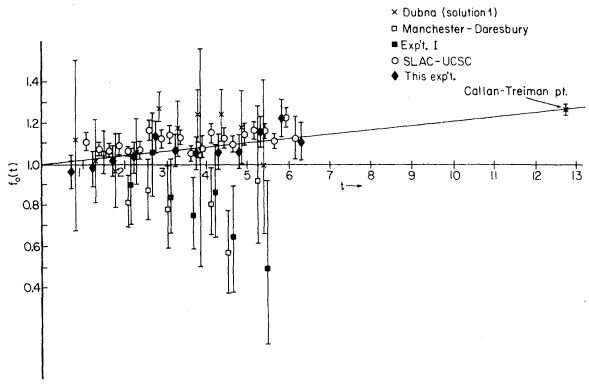

FIG. 15. Comparison of the form factor $f_0(t)$ extracted from various recent experiments: Dubna (cross), Manchester-Daresbury (open square), experiment I (solid square), SLAC-UCSC (open circle), and this experiment (solid diamond).

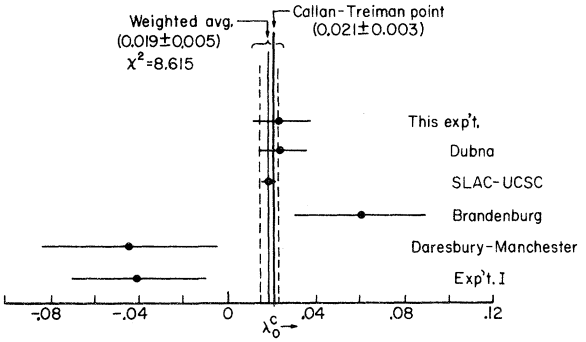

FIG. 16. Comparison of results on the slope parameter λ_0 in constrained linear fits to $f_0(t)$ from recent experiments.

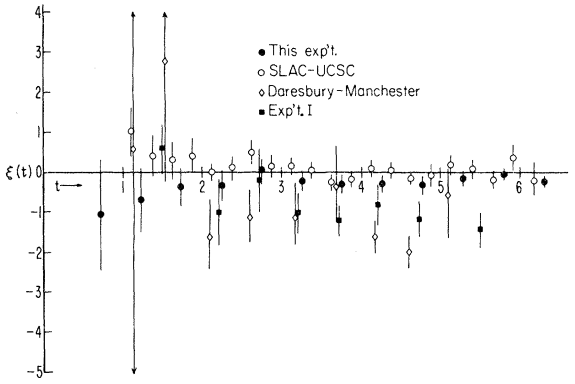

FIG. 17. Comparison of the form factor $\xi(t)$ extracted from various recent experiments: this experiment (solid circle), SLAC-UCSC (open circle), Daresbury-Manchester (open diamond), and experiment I (solid square).

Collaboration of

$$\lambda_+^e = 0.031 \pm 0.0025 \ .$$

3. $f_0(t)$

There are five K_L^0 experiments which have presented f_0 as a function of t: this present experiment, SLAC-UCSC,[8] Dubna,[10] Daresbury-Manchester,[11] and experiment I. Their results are displayed in Fig. 15. The result from each experiment of a constrained linear fit of $f_0(t)$ is displayed in Fig. 16 along with the result of Brandenberg *et al.*[12] A weighted average with a scale factor of 1.3 is dominated by the SLAC-UCSC result and yields

$$\lambda_0 = +0.019 \pm 0.005 \ ,$$

with $\chi^2 = 8.6$ for 5 degrees of freedom.

4. $\xi(t)$

Results of the four K_L^0 Dalitz-plot experiments which presented $\xi(t)$ are shown in Fig. 17. The earlier two experiments (experiment I and Daresbury-Manchester) cluster around -0.8 to -0.5, while the more recent experiment (SLAC-UCSC and this experiment) cluster around 0.0 to -0.3.

---

†Work supported in part by the National Science Foundation and U. S. Atomic Energy Commission.

*Present address: California Institute of Technology, Pasadena, California 91109.
‡Present address: University of Pittsburgh, Pittsburgh, Pennsylvania 15213.
§Present address: Naval Post-Graduate School, Monterey, California 93940.
‖Present address: CERN, Geneva 1211, Switzerland.
¶Present address: Varian Associates, Palo Alto, California 94303.
**Present address: Fermi National Accelerator Laboratory, Batavia, Illinois 60510.
††Present address: University of Pennsylvania, Philadelphia, Pennsylvania 19174.

[1]S. Weinberg, Phys. Rev. Lett. 4, 87 (1960).
[2]For example, T. D. Lee and C. S. Wu, Annu. Rev. Nucl. Sci. 16, 511 (1966).
[3]L. M. Chounet and M. K. Gaillard, CERN Report No. CERN 70-14, 1970 (unpublished); Phys. Rep. 4C, 199 (1972); CERN Report No. Th 1693-CERN, 1973 (unpublished).
[4]C. D. Buchanan *et al.*, Phys. Lett. 33B, 623 (1970); C.-Y. Chien *et al.*, Phys. Lett. 33B, 627 (1970); C.-Y. Chien *et al.*, *ibid.* 35B, 261 (1971); C.-Y. Chien *et al.*, *ibid.* 41B, 647 (1972).
[5]R. H. Dalitz, Proc. Phys. Soc. A69, 527 (1956).
[6]E. S. Ginsberg, Phys. Rev. 171, 1675 (1968); 174, 2169 (1968); Phys. Rev. D 1, 229 (1970).
[7]C. G. Callan and S. B. Treiman, Phys. Rev. Lett. 16, 153 (1966); and R. Dashen and M. Weinstein, *ibid.* 22, 1337 (1969).
[8]G. Donaldson *et al.*, Phys. Rev. D 9, 2960 (1974).
[9]Particle Data Group, V. Chaloupka *et al.*, Phys. Lett. 50B, 1 (1974).
[10]Dubna-Budapest-Berlin-Prague-Serpukhov-Sofia Collaboration, K. F. Albrecht *et al.*, Phys. Lett. 48B, 393 (1974). Solution 1 is quoted here.
[11]M. G. Albrow *et al.*, Nucl. Phys. B44, 1 (1972).
[12]G. W. Brandenberg *et al.*, Phys. rev. D 8, 1978 (1973).